Macromolecules

pubs.acs.org/Macromolecules Article

Dynamical Properties of Concentrated Suspensions of Block Copolymer Stars in Shear Flow

Diego Jaramillo-Cano, Manuel Camargo, Christos N. Likos, and Ioana C. Gârlea*

Cite This: *Macromolecules* 2020, 53, 10015−10027

Read Online

ACCESS | Metrics & More | Article Recommendations

ABSTRACT: Block copolymer stars (BCSs) have been demonstrated to constitute versatile, self-assembling building blocks with tunable softness, functionalization, and shape. We investigate the dynamical properties of suspensions of short-arm BCSs under linear shear flow by means of extensive particle-based multiscale simulations. We determine the properties of the system for representative values of monomer packing fraction ranging from semidilute to concentrate regimes. We systematically analyze the formed network structures as a function of both shear rate and packing fraction, the reorganization of solvophobic patches, and the corresponding radial correlation functions. Connecting our findings with rheology, we calculate the viscosity as a function of shear rate and discuss the implications of the found shear thinning behavior.

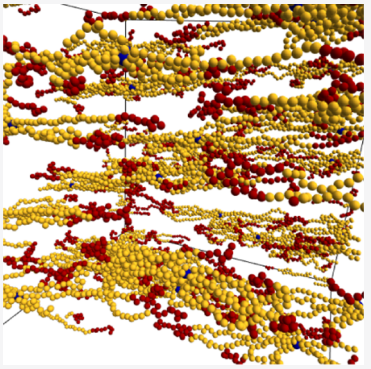

1. INTRODUCTION

The design of novel building blocks for steering the self-assembly of supramolecular systems is currently an expanding research topic because of the wide range of practical applications that could be realized thanks to the possibility of tuning their microstructure, dynamics, and phase behavior. Remarkable examples of such systems are block copolymers, which consist of two or more monomer types polymerized sequentially as covalently linked blocks. These can associate hierarchically in a selective solvent into different configurations that can be systematically modified through different ways, for example, by changing the composition and local distribution of the blocks, solvent quality, or temperature. Depending on the number of blocks and their chemistry, a huge variety of block combinations and polymer architectures are possible nowadays, which self-assemble in solution into structures including spherical and cylindrical micelles, bilayer sheets, vesicles, and Janus nanoparticles.[1−3]

As a particular case, amphiphilic diblock copolymers with a starlike architecture [block copolymer stars (BCSs)] have been proposed in the recent years as a tunable, soft, and flexible realization of patchy particles,[4,5] the latter consisting of rigid colloidal particles decorated with distinct functionalized spots (patches) on their surface. BCSs are formed by at least three linear polymer arms covalently bonded to a central core (anchor), whose size is small in comparison to the arm contour length. At the same time, each arm consists of an amphiphilic AB diblock copolymer with an athermal and solvophilic segment close to the anchor (A-type monomers), followed by thermosensitive and solvophobic monomers (B-type) at the outermost segment. We denote the number of block copolymer arms of the star with f, also known as the functionality of the same, and the fraction of solvophobic monomers in each arm with α. Because BCSs can display both intramolecular and intermolecular association processes, a great deal of work has been devoted to the study of their conformational features, as well as the structure of their suspensions in equilibrium. Examples of experimental realizations of such macromolecules are zwitterionic polybutadiene star polymers and polybutadiene/polyisoprene, poly(acrylic acid)/polystyrene, and poly(ethylene oxide)/poly(propylene oxide) BCSs.[6−10]

Closely related systems to the model described above are aqueous suspensions of tetronic polymers, that is, four-armed (PEO-PPO) star-block copolymers, that, depending on temperature, self-assemble into spherical or rodlike micelles, which in turn form ordered mesophases with fcc cubic and hexagonal structures, respectively.[8] Additionally, the mixtures of end-functionalized, four-armed poly(ethylene glycol) stars display reversible sol−gel transitions in water, which are highly pH-dependent, possess better mechanical properties than randomly cross-linked analogues, and are able to self-heal at low pH.[11]

Received: June 10, 2020
Revised: October 2, 2020
Published: November 12, 2020

https://dx.doi.org/10.1021/acs.macromol.0c01365
Macromolecules 2020, 53, 10015−10027

As mentioned before, recent simulation studies have shown that isolated BCSs can self-assemble into configurations featuring one or multiple clusters of B-monomers (patches) on the outermost region of the star. The equilibrium properties of the formed patches, that is, their number, spatial extent, and number of arms involved, as well as their angular and radial distributions, can be readily and precisely tuned by changing the number of arms (functionality, f), the ratio between the number of solvophobic and solvophilic monomers (amphiphilicity, α), and the strength of the attractive interaction between B-monomers, which models the solvent quality.[5] On the other hand, changes in the same parameters in dilute solutions of BCSs may lead the system to microphase separation, that is, the assembly of micelle-like aggregates, macrophase separation, that is, demixing, or the formation of percolating networks.[12,13]

In the latter case, the competition between attraction strength and amphiphilicity can drive solutions of low-functionality BCSs ($f \lesssim 10$) to form disordered percolating networks, either transient or arrested ones, which are highly homogeneous in the sense that both association sites (patches) and cores are uniformly distributed in space and also that the patches are not broadly polydisperse in size.[13] The homogeneity of the network is a consequence of the reconfigurable nature of the BCSs, which acquire a much more open and isotropic average configuration as the concentration increases in comparison to the isolated case, maximizing the inter-star associations and displaying short- and intermediate-range ordering at the monomer- and macromolecule-length scales, in close similarity with the findings on telechelic linear polymers. Because the analyzed systems are assumed to be nonentangled, from the structural point of view, these BCSs are appropriate candidates for the assembly of homogeneous, reversible polymer gels, which could exhibit fascinating properties such as stimuli responsiveness, self-healing, and shape memory.[14,15]

From a general dynamical point of view, the behavior of dilute solutions of associative polymers is mainly determined by intramolecular associations, while in the semidiluted nonentangled regime, where an interplay between inter- and intramolecular associations takes place, viscoelastic properties are expected to be characterized by at least two time scales, that is, the typical time for formation and breakage of intermolecular associations and the relaxation time of intramolecular chain segments.[16] Of course, these factors influence the response of the system under nonequilibrium conditions. For example, telechelic, linear polymers assemble in equilibrium into scaffold-like networks, whose properties are governed by the polymer flexibility and end attraction strength.[17] In these systems, shear flow induces significant (reversible) structural changes, which can be associated with major rheological regimes which, depending on the strength of the applied shear flow, include Newtonian behavior, shear banding, and shear thinning.[17−19] This behavior is also common to a large variety of polymer-based soft colloids, such as multiarm stars and microgels.[20]

In isolated BCSs, the shear can be utilized as yet another parameter for tuning the intramolecular self-assembly behavior. The shear increases the patchiness of low-amphiphilic-fraction BCSs, that is, $\alpha \lesssim 0.3$, as a result of their alignment with the flow field, while for high-amphiphilic-fraction stars, that is, $\alpha \gtrsim 0.7$, the number and size of patches formed are nonmonotonic functions of shear rate. The key factors in determining the evolution of the star's patchiness and global configuration under shear are the presence of nonassociated arms and the spatial extent of the patches. Depending on these factors, the main mechanisms for patch evolution under shear involve the merging of free arms into new patches, the joining of two patches into one, and the split-off of bulky patches under strong shear.[21] On the other hand, for semidilute solutions of low-functionality telechelic star polymers ($f \leq 3$), which also form connected networks, an increasing viscosity is predicted as the concentration, functionality, or the attraction between B-monomers increases.[10,22] Furthermore, the steady-state response of these solutions under shear flow features both Newtonian and shear thinning behaviors, the latter being linked to the fission of inter- and intra-star patches.

The aforementioned examples show how differences in the structure of associating polymers give rise to large changes in their properties. Until now, studies under shear flow have been carried out for three- or four-armed BCSs. Because it is expected that higher-functionality BCSs facilitate the formation of stiffer networks than lower-functionality BCSs and similar mass,[6] the aim of this work is to complement our previous in-equilibrium study of network-forming BCSs of moderate functionality.[13] We systematically analyze the effect of shear flow on the global structure and molecular conformations of the BCSs in reversible percolating systems, which are not too dense yet topologically interesting. For these systems, our results suggest that the orientation and elongation of the BCSs induced by the shear flow give rise to reorganization of both the patchiness and network connectivity, leading to shear thinning behavior with the thinning exponent growing in magnitude with the concentration of the solution.

The rest of the paper is organized as follows: in Section 2, we briefly present the model and simulation technique employed. Section 3 is devoted to extensively present and discuss our results regarding the conformation properties, patchiness, and viscosity of the system as a function of shear rate and packing fraction. Finally, in Section 4, we summarize and draw our conclusions.

2. MODEL AND METHODS

2.1. BCS Model. We simulate BCSs through a bead-spring model with monomers being soft spheres of diameter σ and mass M. Following our previous work,[13] simulations were performed on BCSs of functionality $f = 9$ and a polymerization degree $N = 30$ for each arm. The arms are all connected to a central bead (anchor) of diameter $\sigma_a = 1.5\sigma$ and mass M. The inner block of each arm (i.e., the one placed toward the anchor) behaves like a polymer under good solvent conditions (solvophilic monomers), while the outer block is solvophobic, that is, monomers of this type attract each other. The solvophobic monomers will be referred to as B-monomers, whereas the solvophilic ones will be denoted as A-monomers. The fraction of B-monomers determines the amphiphilicity α and is defined as $\alpha = N_B/N$, where N_B is the number of B-monomers in each arm and $N = N_A + N_B$. In the following, we focus on two cases: $\alpha = 0.3$ and $\alpha = 0.5$.

The interaction between monomers is constructed based on the generalized Lennard-Jones potential

$$V(r) = 4\epsilon\left[\left(\frac{\sigma}{r}\right)^{48} - \left(\frac{\sigma}{r}\right)^{24}\right] \quad (1)$$

where ϵ and σ set the energy and length units, respectively. By shifting and truncating it in the Week−Chandlers−Anderson fashion, the interaction potential between A-monomers and the one between A and B monomers reads

https://dx.doi.org/10.1021/acs.macromol.0c01365
Macromolecules 2020, 53, 10015−10027

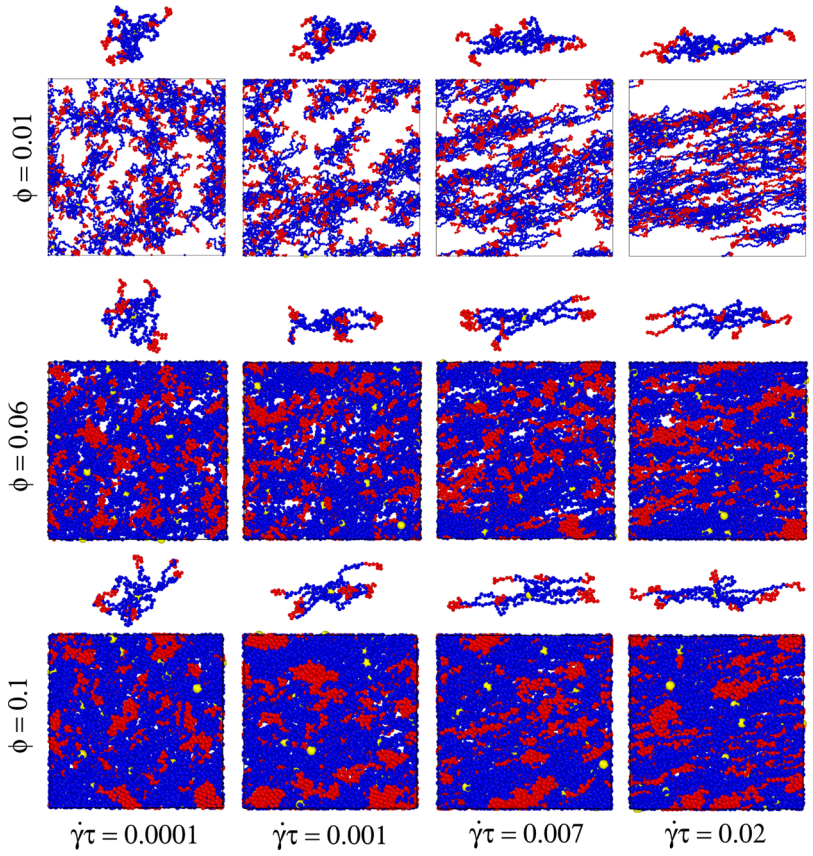

Figure 1. Snapshots from simulation for BCS solutions with $\alpha = 0.3$ at different volume fractions ϕ and shear rates $\dot{\gamma}$. The solvophilic monomers are shown in blue, solvophobic monomers in red, and anchors in yellow. Above each image, one star selected at random is shown separately to make the typical shape of a BCS visible. The number of stars in all boxes is the same, but the boxes have different sizes according to the density; therefore, the stars at lower densities appear smaller in the snapshots. The snapshots of the single stars are all drawn at the same scale to facilitate shape and size comparisons.

$$V_{AA}(r) = V_{AB}(r) = \begin{cases} V(r) + \epsilon & r \le r_{cut} \\ 0 & r > r_{cut} \end{cases} \quad (2)$$

where $r_{cut} = 2^{1/24}\sigma$ is the cutoff distance. The interaction between an anchor and another monomer (regardless of type A or B) is given by the same functional form with σ replaced by $\sigma' = (\sigma + \sigma_a)/2 = 1.25\sigma$. For the interaction between B-monomers, we define the following potential

$$V_{BB}(r) = \begin{cases} V(r) - \epsilon(\lambda - 1) & \text{for } r \le r_{cut} \\ \lambda V(r) & \text{otherwise} \end{cases} \quad (3)$$

with λ the parameter employed for controlling the strength of the attractive contribution.[5] For the rest of our study, we consider the case $\lambda = 1.2$ only. The reason for this choice is based on our previous equilibrium studies on BCS network formation.[13] For $f = 9$, $N = 30$, and the α-s considered, single isolated stars are only partially self-assembled, indicating that there are some arms clustered together by their attractive segments while others are unbounded. We also note that although the model employed here is the same as the one used by Rovigatti et al.,[5] the single-star configuration there is different for $f = 9$ and $\lambda = 1.2$ because stars with much longer arms ($N > 120$) are considered in that work. For the systems in hand, as the stars are brought at higher concentration, they form percolating networks where multiarm aggregates coexist with free arms.[13] Unlike at higher attraction strengths, at $\lambda = 1.2$, the arms can unbind and rebind relatively fast compared to our simulation time, and therefore, the network permanently reorganizes, but it maintains its overall structure. We expected that this type of network will have interesting self-healing properties when disrupted by external factors such as shear.

In addition to the Lennard-Jones-like potential, adjacent monomers in the same arm of the star are bonded by a finitely extensible nonlinear elastic (FENE) potential of the form

$$V_b(r) = -15\epsilon\left(\frac{R_0}{\sigma}\right)^2 \ln\left[1 - \left(\frac{r}{R_0}\right)^2\right] \quad (4)$$

where $R_0 = 1.5\sigma$ denotes the maximum separation allowed between two beads; as before, for the anchor-arm bond, σ is replaced by σ'.

2.2. Simulation Technique. To accurately simulate our system, we make use of a hybrid simulation technique, which combines monomer-resolved molecular dynamics (MD) for the polymers and a coarse-grained representation of the solvent by means of multiparticle collision dynamics (MPCD), which models the solvent at the Navier−Stokes level and introduces hydrodynamic interactions between monomers.[23,24] A standard version of MD is employed based on the Verlet integration scheme[25] with a time step $\Delta t = 10^{-3}\,\tau$, with τ being the microscopic time unit defined below. On the other hand, MPCD models the solvent as composed of point particles whose dynamics follows two steps: during the streaming step, the solvent particles propagated ballistically, while in the collision step, they exchange linear momentum among them and the monomers. The latter proceeds by splitting the simulation box into cubic cells of size $a = \sigma$ and then the relative velocity of all particles in each cell (with respect to the velocity of the cell's center of mass) is rotated by an angle $\chi = 130°$ around a randomly chosen axis. A random shift of the collision cells is applied at any collision step to guarantee Galilean invariance.[26]

https://dx.doi.org/10.1021/acs.macromol.0c01365
Macromolecules 2020, 53, 10015−10027

We consider an average of $\rho = 5$ solvent particles of mass $m = M/5$ per collision cell, where m sets the unit of mass.[21] The time between two collision steps is defined as $h = 0.1\ \tau$, where $\tau = \sqrt{m\sigma^2/\epsilon}$ is the time unit. By using a Maxwell−Boltzmann cell-level thermostat, the absolute temperature of the system is kept constant at $k_BT = 0.5\ \epsilon$, where k_B is the Boltzmann constant. In this way, the solvent viscosity results $\eta_s \simeq 4.1(\sqrt{m\epsilon}/\sigma^2)$. In order to induce a shear (planar Couette) flow on the pure solvent, Lees−Edwards boundary conditions are applied to the simulation box, which lead to a velocity profile $\boldsymbol{v} = \dot{\gamma}y\hat{\boldsymbol{x}}$, with $\dot{\gamma}$ being the shear rate.[27,28]

In our simulations, we choose to keep the number of stars fixed ($N_s = 35$), and in order to change the concentration of stars, we vary the box size L_{box}. We focus our study on three particular values for the (monomer) volume fraction $\phi = 0.01$, 0.06, and 0.1, which is defined as $\phi = N_sV_0/{L_{box}}^3$, where $V_0 = (\pi/6)\ (Nf\sigma^3 + \sigma_a^3)$ is the volume occupied by the monomers of each star. The lowest volume fraction corresponds to a dilute regime in which stars interact, forming small inter-star associations. At the intermediate ϕ, the BCSs form in equilibrium a percolating network even if this volume fraction accounts only for around 65% of the polymer overlap concentration ϕ^*. The latter is defined as

$$\phi^* = V_0\left[\frac{4}{3}\pi(R_{gyr}^{(at)})^3\right]^{-1} \tag{5}$$

with $R_{gyr}^{(at)}$ denoting the gyration radius of an isolated athermal star polymer (i.e., $\alpha = 0$) at equilibrium. Finally, the highest ϕ-value lies above the overlap concentration ($\phi \simeq 1.12\phi^*$), where well-formed gels are obtained.[13] Using the mean-square displacement of the anchors measured in equilibrium, we established that the system is fluid for all parameters considered in this study, except for $\alpha = 0.5$ at $\phi = 0.06$ and $\phi = 0.1$, where it shows signs of being arrested.

The shear rates $\dot{\gamma}$ considered in this work lie in the range between $10^{-4}\ \tau^{-1}$ and $4 \times 10^{-2}\ \tau^{-1}$. To facilitate comparison with other results, the shear rate can be expressed by the Weissenberg number via the relation $Wi_0 = \dot{\gamma}\tau_Z$, with τ_Z being a characteristic relaxation time. In this work, $\tau_Z = \eta_S\sigma^3N^{3\nu}f/(k_BT)$ corresponds to the longest Zimm relaxation time for an arm of an athermal star ($\alpha = 0$) with η_s and $\nu_f = 3/5$ being, respectively, the viscosity of the solvent and the Flory exponent for self-avoiding chains.[29,30] In this way, $\tau_Z \approx 7.5 \times 10^3\ \tau$, and consequently, the range of Weissenberg numbers covered goes from $Wi_0 \simeq 0.75$ to $Wi_0 \simeq 300$.

Last, four independent runs for each considered set of parameters $\{\alpha, \phi, \dot{\gamma}\}$ were performed. The equilibrated samples obtained from MD-MPCD hybrid simulations without shear were used as a starting configuration of nonequilibrium simulations. In the latter case, the system was left to reach steady state during $t_{ss} = 5 \times 10^3\ \tau$ after which a production stage took place at least for $t_{prod} = 5 \times 10^4\ \tau$. All data presented in the remaining of this work was measured in steady-state flow. We therefore observe no changes of the measured quantities with time.

3. RESULTS AND DISCUSSION

3.1. General Behavior under Shear. We begin our discussion by describing the behavior of our BCS system at different amphiphilicities α and volume fractions ϕ as a function of shear rate $\dot{\gamma}$. At $\alpha = 0.3$, for the lowest monomer fraction ($\phi = 0.01$) and the lower shear rates considered ($\dot{\gamma}\tau \lesssim 0.001$), there are no effects of the flow observed (see the upper left panels of Figure 1), neither at the level of the single stars (i.e., the shape of the stars appears, at least by eye, to be the same as in equilibrium) nor at the level of inter-star aggregates (i.e., the average number of BCSs that are connected does not seem to change, even if arms unbind and rebind continuously). At $\dot{\gamma}\tau = 0.001$, we start being able to distinguish stars flowing along the field. The stars still do not change shape appreciably and each inter-star cluster flows with a constant velocity, keeping its equilibrium morphology. For $\dot{\gamma}\tau = 0.004$ ($Wi_0 \approx 30$), we begin to observe elongations at the level of single stars along the flow direction, combined with the flattening of the star shape in the xz-plane that becomes more visible as $\dot{\gamma}$ increases. The star clusters also start to change the shape, with their elongation also being in the flow direction. Above $\dot{\gamma}\tau = 0.02$ shear banding can be seen, as shown in the upper right panels of Figure 1.

At the intermediate volume fraction $\phi = 0.06$, the percolating network that characterizes our system in equilibrium is, as in the case of lower monomer fraction, largely undisturbed when low shear rates are applied (Figure 1, middle row). As the shear rate increases, the size of the attractive aggregates built by different arms coming together starts to decline because arms are being pulled out from the aggregates by the flow. Similar to the system at low density, for $\dot{\gamma}\tau \gtrsim 0.004$, we observe stretching of the polymers, accompanied by elongation of the attractive aggregates. The network appears to percolate for all $\dot{\gamma}$ values considered in this study. The most dense system analyzed ($\phi = 0.1$) shows a similar behavior than the one at $\phi = 0.06$, with the difference that here the attractive aggregates stretch already at a lower shear rate ($\dot{\gamma}\tau = 0.001$ compared to $\dot{\gamma}\tau = 0.002$), as shown in the top panels of Figure 1.

For the case $\alpha = 0.5$, the behavior is similar to the corresponding system at lower α, with the particularity that here we observe ruptures of the network, that is, our initially percolating systems ($\phi = 0.06$ and $\phi = 0.1$) break down into multiple disconnected subcomponents. This phenomenon is due to the topology of the network in equilibrium: the systems at this attractive monomer fraction have large free voids inside the network.[13] Then, as shear is applied, the places of the network where the network is weaker, that is, where the inter-star connections are minimal being formed by just one arm coming from each star, will break apart.

3.2. Geometrical Properties. A more quantitative description of the observed conformational changes of a BCS under shear can be provided by the analysis of its gyration tensor $\mathbb{G}$, whose entries are defined as

$$\mathbb{G}_{\mu\nu} = \frac{1}{N_{mon}}\sum_{i=1}^{N_{mon}}(r_{i,\mu} - r_{cm,\mu})(r_{i,\nu} - r_{cm,\nu}) \tag{6}$$

where $r_{i,\mu}$ and $r_{cm,\mu}$ are the μ component ($\mu = x, y, z$) of the i-th monomer and of the star center of mass instantaneous positions, respectively, and $N_{mon} = f\ N + 1$. The three eigenvalues of $\mathbb{G}$, $\lambda_1 > \lambda_2 > \lambda_3$, can be used to construct the invariants $I_1 = \lambda_1 + \lambda_2 + \lambda_3$, $I_2 = \lambda_1\lambda_2 + \lambda_2\lambda_3 + \lambda_1\lambda_3$, and $I_3 = \lambda_1\lambda_2\lambda_3$, which can be used as shape descriptors of the polymers.

The first invariant can be linked to the gyration radius of the BCS via the relation $R_{gyr} = \sqrt{\langle I_1\rangle}$, where angular brackets denote an average over all molecules and time. Similarly, we can compute the asphericity δ, the prolateness S, and the acylindricity c.[31−33] The asphericity δ is defined as

$$\delta = 1 - 3\left\langle\frac{I_2}{I_1^2}\right\rangle$$

which takes values between 0 and 1, with the minimum value describing an object with a perfect spherical symmetry. On the other hand, the prolateness S reads

https://dx.doi.org/10.1021/acs.macromol.0c01365
Macromolecules 2020, 53, 10015−10027

$$S = \left\langle \frac{1}{I_1^3} \prod_{i=1}^{3} (3\lambda_i - I_1) \right\rangle \tag{7}$$

with its value ranging from −0.25 to 2, where the negative values indicate oblate shapes, whereas the positive ones map to prolate objects. Last, the acylindricity c can be computed as

$$c = \left\langle \frac{\lambda_2 - \lambda_3}{I_1} \right\rangle \tag{8}$$

which is a positively defined quantity with $c = 0$ describing a perfect cylindrical symmetry.

The first finding to point out regarding the shape parameters is that the volume fraction of monomers has an effect on the gyration radius even for low shear rates: the BCSs that are part of denser systems increase by a larger proportion relative to their equilibrium configuration, see Figure 2a. This is a consequence of the fact that, for $\phi = 0.06$ and $\phi = 0.1$, the BCSs form a percolating network, and even a small deformation of system leads to extension of the individual stars. At $\phi = 0.01$, where the inter-star interaction is reduced, the relative size of the stars is around the same as for single star. At low shear rates, the asphericity δ is higher for stars with $\alpha = 0.5$ than for these with $\alpha = 0.3$ (data not shown) because the stars with more functionalized monomers form more asymmetric structures, that is, a higher number of B-monomers are localized in the attractive aggregates. As the shear rate increases, the curves for both values of α collapse. This is an indication of the unfolding of the attractive aggregates. The prolateness S goes up with $\dot{\gamma}$, whereas the acylindricity c decreases, see Figure 2b,c, which is consistent with the observation that the BCS stretch, having a more cigar-like shape as the system is sheared. Both of these shape parameters also display collapse of different α-systems at high $\dot{\gamma}$, consistent with a fully elongated polymeric star. The higher the density, the more elongated the stars become because of the inter-star connections that have to be accommodated in addition to the flow.

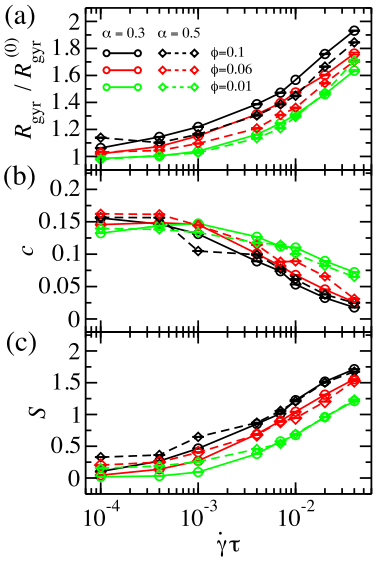

Figure 2. Global shape parameters of BCSs as a function of shear rate for different concentrations and amphiphilicities: (a) normalized gyration radius $R_{gyr}/R_{gyr}^{(0)}$, (b) acylindricity c, and (c) prolateness S. The value $R_{gyr}^{(0)}$ denotes the gyration radius of an isolated BCS at equilibrium.

To obtain more information on the deformations of the BCSs with respect to the spatial directions, we analyze the diagonal components $G_{\mu\mu} = \langle \mathbb{G}_{\mu\mu} \rangle$ of the gyration tensor normalized to the value of isolated BCS at equilibrium, $G_{\mu\mu}^{(0)}$, as shown in Figure 3a−c. At $\phi = 0.01$, the system shows a behavior similar to that of isolated stars:[21] for low shear rates ($\dot{\gamma}\tau < 4 \times 10^{-4}$), no strong deformation appears; as $\dot{\gamma}$ increases, both monotonically increasing G_{xx} and diminishing G_{yy} are found, reaching a difference of almost one order of magnitude with respect to $G_{\mu\mu}^{(0)}$ at the highest $\dot{\gamma}$ probed; meanwhile, G_{zz} decreases only slightly. This indicates that the extension of the BCSs occurs along the flow direction (x-direction). Although its size is drastically decreased in the gradient direction (y-direction), the relative shrinkage in the vorticity direction is comparatively small, hinting at a flattened elliptical shape of the BCS located in the xy-plane. As mentioned above, for the higher concentrations, spatial inhomogeneities in the shape of the BCSs with respect to the isolated case are observed even at $\dot{\gamma}\tau = 10^{-4}$ and, at higher shear rate, even lower values for G_{yy} and G_{zz} are found, which points out to a more rodlike shape of the BCSs. It is to be noted that, for each density, the corresponding curves for $\alpha = 0.3$ and $\alpha = 0.5$ collapse at high shear rate.

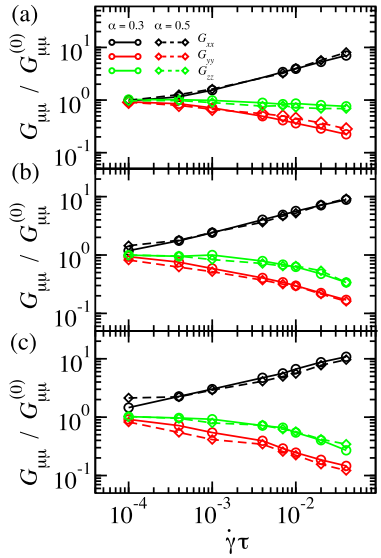

Figure 3. Normalized diagonal components of the gyration tensor $G_{\mu\mu}/G_{\mu\mu}^{(0)}$ as a function of shear rate at different monomer volume fractions: (a) $\phi = 0.01$, (b) $\phi = 0.06$, and (c) $\phi = 0.1$. The quantities $G_{\mu\mu}^{(0)}$ are the averaged diagonal components of $\mathbb{G}$ for an isolated BCS at equilibrium.

Compared to nonaggregating stars ($\alpha = 0$), BCSs show a similar stretching behavior in the flow direction. For isolated stars, the relative stretching in the flow direction is higher for nonaggregating stars than for the functionalized ones and decreases with the increases in functionalization fraction α.[21] At finite densities, for athermal stars, the relative stretching in the flow direction G_{xx} varies very little with respect to the density for the values considered in our study,[34] as opposed to BCSs. For BCSs at $\phi = 0.01$ and the higher shear rates considered, the relative stretching in the flow direction is lower than the one reported for athermal stars. At the intermediate monomer fraction $\phi = 0.06$, G_{xx} takes values similar to the

https://dx.doi.org/10.1021/acs.macromol.0c01365
Macromolecules 2020, 53, 10015−10027

ones for athermal stars, whereas at $\phi = 0.1$, the BCSs are more extended.

The geometrical properties of our stars are the result of a compromise between self-assembly and flow alignment. In the dilute regime, the functionalized stars extend less (than athermal ones) in order to be able to keep their patches. When the density increases and a network is formed, the BCSs are, in addition, subject to the pulling exerted by the neighboring stars to which they are connected and which also try to align to the flow. This leads to a higher relative increase in size in the flow direction.

The elongation of star polymers along the flow direction is not an unusual behavior in polymeric systems subjected to shear or flow. It appears for a multitude of other polymeric architectures such as linear chains,[35−38] branched chains,[39,40] and rings[41,42] and spans a wide range of concentrations from dilute to melts. Each system has its particularities; however, the orientation and extension in the direction of the flow is a common trend that makes these polymeric systems, to a certain degree, lookalike. Our systems bear interesting similarities to colloidal gels, even if the two systems are very different in many other respects. The stretching and reorientation of the BCS arms under flow looks surprisingly similar to the deformations appearing in sheared colloidal gels.[43,44]

Further insights into the positioning of the BCS with respect to the flow can be gained by considering the orientational resistance m_G. This parameter measures the average alignment of the BCS induced by the flow and it is related to the angle χ_G formed by the eigenvector $\hat{\mathbf{e}}_1$ associated with the largest eigenvalue λ_1 of $\mathbb{G}$ and the flow direction. It is defined in terms of the components of the gyration tensor as[29]

$$m_G = W_i \tan(2\chi_G) = W_i \frac{2G_{xy}}{G_{xx} - G_{yy}} \tag{9}$$

As displayed in Figure 4a, the orientational resistance increases with $\dot{\gamma}$. For the two higher densities, we observe a reasonably fair overlap of the curves, while the dilute system features a higher orientational resistance than the denser counterparts.

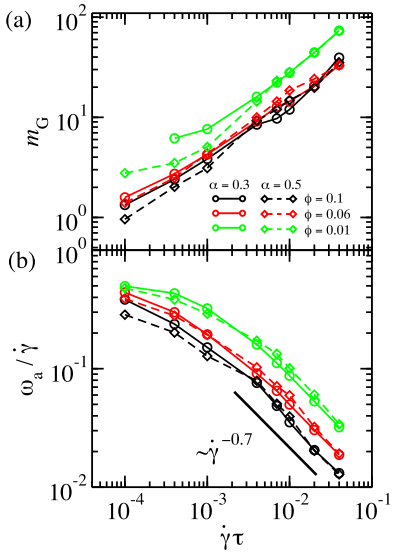

Figure 4. (a) Orientational resistance and (b) apparent angular velocity as a function of shear rate.

This phenomenon can be again explained by the larger connectivity of the denser system. There, the alignment along the flow direction is further enhanced and also stabilized through the connection of attractive B-monomers at the end of each arm with abundant neighboring ones from the surrounding BCSs.

Furthermore, to understand the dynamics of the stars, we can make use of the angular velocity which we define as

$$\omega_a = -\dot{\gamma} \frac{G_{yy}}{G_{xx} + G_{yy}} \tag{10}$$

For isolated BCSs, it can be interpreted either as the tumbling frequency of a rigid body in the shear flow, whose shape is similar to the average shape of the BCS, or as the frequency at which the individual arms rotate by tank-treading around the geometrical star center.[45] As can be seen in Figure 4b, the ratio between the angular velocity and the shear rate ($\omega_a/\dot{\gamma}$) decreases as the latter increases, which is due to the flexibility of the BCS: for a rigid object, we expect to have $\omega_a/\dot{\gamma}$ constant, whereas here clearly $\omega_a/\dot{\gamma} \propto \dot{\gamma}^{-a}$, with $a \simeq 0.7$ for the larger shear rates probed. Also, we observe that lower densities allow for higher ω_a because stars exhibit less steric hindrance from neighbors and also are less likely to break free from inter-star connection and to tumble because they have fewer of these connections per star.

3.3. Radial Correlation Functions. In order to analyze the microscopic conformation of the system, we use radial pair-correlation functions for the different monomer species. In particular, it allows us to gain additional information about the structure of the attractive patches. The pair-correlation function $g_{IJ}(r)$, which assesses the probability of finding a monomer of species I at a distance r from a monomer of species J, is defined as

$$g_{IJ}(r) = \frac{V}{\hat{N}_I \hat{N}_J} \left\langle \sum_{i=1}^{\hat{N}_I} \sum_{j=1}^{\hat{N}_J} \delta(\mathbf{r} - \mathbf{r}_{ij}) \right\rangle \tag{11}$$

where $r = |\mathbf{r}_{ij}|$ denotes the distance between the i-th and j-th monomers.[46,47] The subindexes I and J can take any of the values A for noninteracting monomers, B for functionalized ones, and C for anchors. For g_{II}, the terms with $i = j$ are excluded from the sum. The normalization constants $\hat{N}_A$ represent the total number of A monomers in the system ($\hat{N}_A = N_s f N_A$), $\hat{N}_B$ is the number of functionalized monomers ($\hat{N}_B = N_s f N_B$), whereas $\hat{N}_C = N_s$ is the number of anchors.

We first turn our attention to the pair-correlation function $g_{AA}(r)$ between the nonfunctionalized parts of the stars as presented in Figure 5. At $\alpha = 0.3$ and low shear rates, we observe no significant difference to the equilibrium behavior for very dilute system ($\phi = 0.01$), that is, the radial pair correction function exhibits a first peak at $r/\sigma \simeq 1$, which corresponds to the first-order neighbors along the chain, followed by a much less-pronounced one at $r/\sigma \simeq 2$, see Figure 5a. By increasing the shear rate, an increase in these two peaks takes place. At $\dot{\gamma}\tau = 0.04$, we start seeing regular peaks at approximately integer values of r/σ. These provide evidence of the stretching of the polymers along the flow, forming an ordered structure. The same stretching feature of the A-blocks of the arms is also observed in the $g_{CA}(r)$ correlation function (data not shown). Moreover, the depleted region observed at $r/\sigma \approx 14$ corresponds to the typical size of stars and disappears with the increase in $\dot{\gamma}$ because of the homogenization of the

https://dx.doi.org/10.1021/acs.macromol.0c01365
Macromolecules 2020, 53, 10015−10027

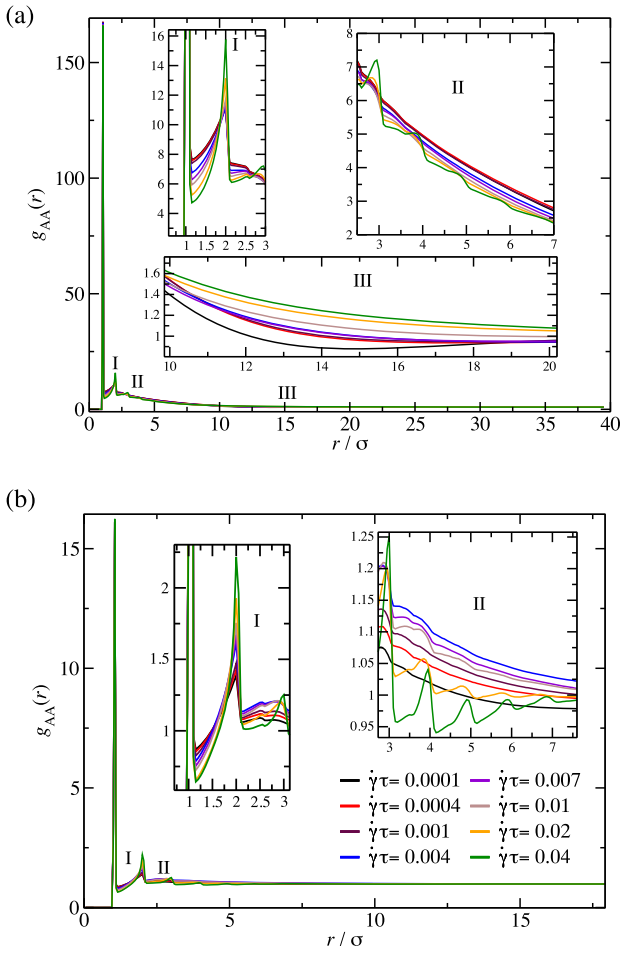

Figure 5. Radial correlation function of A-monomers for (a) $\phi = 0.01$ and (b) $\phi = 0.1$. Insets show enlarged zones of the curves for different radial distances. The data presented in both panels correspond to $\alpha = 0.3$.

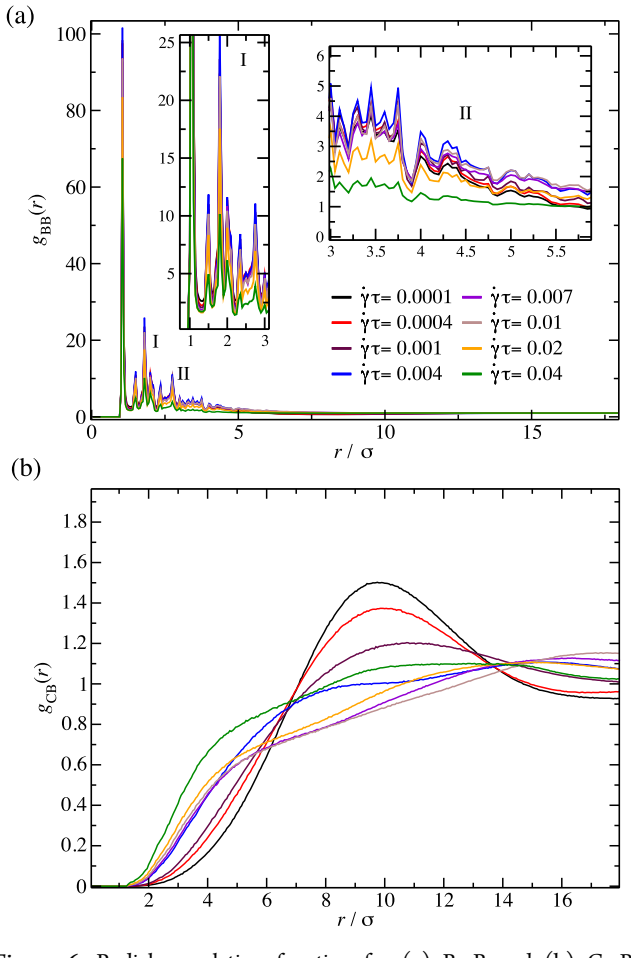

Figure 6. Radial correlation function for (a) B−B and (b) C−B monomer pairs. Insets in panel (a) show enlarged zones of the curves for different radial distance. For both panels, $\alpha = 0.3$ and $\phi = 0.1$.

system. The higher-density systems presented in Figure 5b show the same features as the one at $\phi = 0.01$, with the peaks being more pronounced, which is consistent with the increase in the monomer local density. The depletion region observed for the dilute system is not present at this monomer fraction because each star is here surrounded by multiple other stars. The systems with $\alpha = 0.5$ show similar features, but the peaks of $g_{AA}(r)$ at short distance tend to have higher values because the stars have better formed patches, indicating that the arms are placed closer together. The regular structure at high $\dot{\gamma}$ vanishes at lower r/σ because the noninteracting part of the arms is shorter at $\alpha = 0.5$.

On the other hand, the correlation function ($g_{BB}(r)$) for the attractive monomers features a much more structured profile as shown in Figure 6a. The locations of the correlation peaks are consistent with a random hexagonal close-packed structure. This arrangement has also been observed in equilibrium[13] and is a direct consequence of the short-range attractive interaction between B-monomers. At low density, these peaks decrease in height significantly for $r/\sigma > 2$, which is concomitant with the average size of the observed clusters. For $\phi = 0.06$ and $\phi = 0.1$, the peaks are observable up to a distance $r \simeq 8\sigma$ and decrease in size as the shear rate increases. Particularly visible are the nonmonotonic changes of the peak heights of $g_{BB}(r)$ with shear rate, as can be seen in inset II. Starting from equilibrium, the peaks as well as the magnitude of the radial distribution function first grow until the value $\dot{\gamma} \simeq 0.01$ is reached, arising from the stretching of the arms due to shear and the concomitant proximity of B-type beads along the flow direction. However, as the increasingly high shear brings about a breaking of the transient BB-bonds, the curve flattens dramatically out at the highest shear rate, $\dot{\gamma}\tau = 0.04$. This loss of the connectivity between stars at high shear is confirmed by our subsequent analysis of the system connectivity in Section 3.4.1. At the highest shear rate analyzed $\dot{\gamma}\tau = 0.04$, the peaks at $r/\sigma > 4$ and $r/\sigma > 7$ for $\alpha = 0.3$ and $\alpha = 0.5$, respectively, vanish. Similarly, as the shear rate increases, lower peaks are observed, suggesting that the size of the attractive aggregates decreases as the system is sheared as a consequence of the detachment from the cluster of some arms.

By looking at the pair-correlation function between noninteracting and functionalized monomers ($g_{AB}(r)$), we notice significant peaks only at $r/\sigma \simeq 1$ and $r/\sigma \simeq 2$ at zero shear. At high shear rates, $g_{AB}(r)$ develops a profile with multiple peaks located at integer values of r/σ, this again being an indication of chain stretching (data not shown). The stretching is also supported by the anchor-functionalized monomer correlation function $g_{CB}(r)$ shown in Figure 6b. As can be seen there, the equilibrium $g_{CB}(r)$ shows a well-defined peak around $r/\sigma \simeq 8-10$ depending on ϕ. This distribution flattens out as shear increases, leading to an increasing value at shorter r due to the induced elongation of the arms B-block.

https://dx.doi.org/10.1021/acs.macromol.0c01365
Macromolecules 2020, 53, 10015−10027

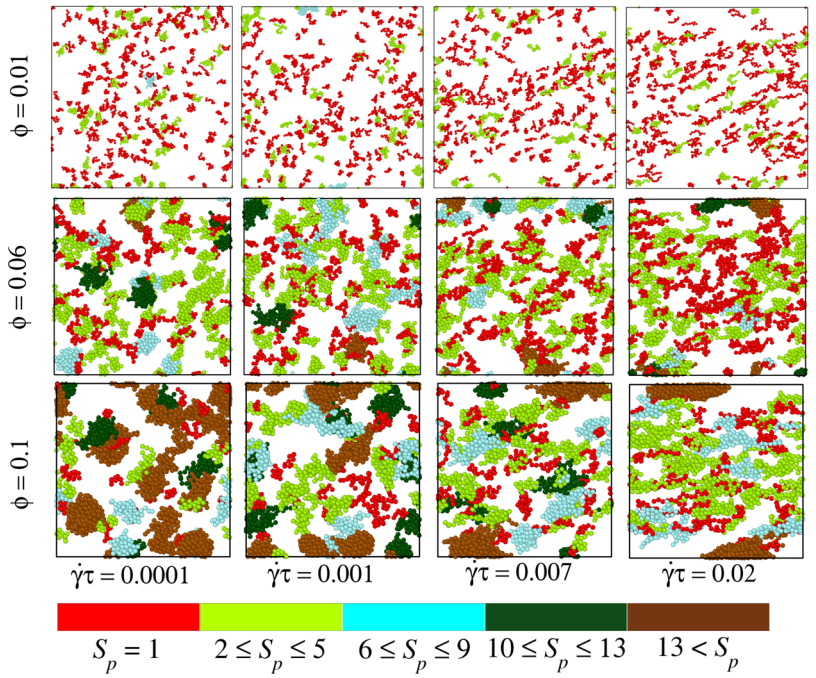

Figure 7. Graphical representation of the patch size behavior for α = 0.3, different density (ϕ), and shear rate ($\dot{\gamma}$). Here, only B-monomers are displayed. Each color categorizes the size S_p of the patches: red is used for free arms (S_p = 1), whereas green, light blue, dark green, and brown denote small, medium, large, and giant patches, respectively.

Because the BCSs align with the flow, a new space is open, which can be occupied by another stars. A similar phenomenon is also seen in the anchor−anchor correlation function $g_{CC}(r)$, where anchors are allowed to come closer as the shear increases.

The information given by our pair-correlation functions can be experimentally accessed using rheo-SANS as it has been shown with starlike[48] and wormlike micelles.[49−51] The rheo-SANS measurements allow for detection of anisotropy in reciprocal space, which can be related to our pair-correlation functions in real space. In the case of starlike micelles, the rheo-SANS experiments show an increase in both the structure factor and inter-micelle distance, which can be directly associated with the increase of shear rate. These changes occur along both the flow and the vorticity directions and can be rationalized by an elongation of the micelles together with a tilt with respect to the flow lines.[48]

3.4. Patch Behavior. In the previous section, we presented results regarding the global conformation properties of the systems under consideration. Now, we turn our attention to the effect of shear on the features of the formed attractive aggregates (patches), in particular, to the number of patches in the system (N_p) and their size (S_p), that is, the number of arms clustered in each patch. A patch is defined as the set of functionalized monomers that have the property that any monomer in the patch is located at a maximum distance d = 1.08σ from at least one other monomer in the patch. This definition implies that all attractive monomers in an arm are part of the same patch. In order to be part of the same patch, two arms do not need to have direct "contact", but any of their monomers can be placed closer than d to functionalized monomers of another arm or other arms that have contact to each other.[13]

At this point, it is important to note that the average configuration of isolated BCSs at equilibrium that we found features the coexistence of free arms and patches. This behavior is different from the fully self-assembled scenario, that is, no presence of free arms, described by Rovigatti et al.,[5] for similar parameters (f, α, and λ). This difference is a consequence of the large arm polymerization degrees employed there (N > 120) in comparison to the much shorter arms (N = 30) we consider here, which in turn leads to a higher steric penalty when forming patches. In fact, the BCSs considered here become fully self-assembled as λ increases.[13]

In this way, at low density, a large fraction of the arms are free because potential binding partners are spatially far away, whereas at higher densities, more arms are bound, leading to the increase of the size S_p of the equilibrium clusters. Aiming to visualize the changes in cluster size due to different parameters, we divided the clusters into five size categories: free arms, small clusters involving 2−5 arms, medium clusters which are composed of 6−9 arms, large clusters with 10−13 arms, and giant clusters containing more than 13 arms. Each category is assigned a different color in Figure 7. For low density (ϕ = 0.01) and $\dot{\gamma}\tau \leq$ 0.007, the cluster size does not drastically change, the system has mostly free arm, a population of small clusters, and few medium-sized ones, whereas at $\dot{\gamma}\tau$ = 0.02, the medium-sized clusters have vanished. For the other densities, the largest cluster size (large for ϕ = 0.06 and giant for ϕ = 0.1) persists at low $\dot{\gamma}$, but it vanishes at $\dot{\gamma}\tau$ = 0.007. The further increase in $\dot{\gamma}$ leads to the disappearance of the next cluster size population. It is also interesting to note how the clusters elongate as the system is sheared, as well as that free arm extend more than clusters since the energetic loss is smaller.

To have a quantitative measure of the change in cluster size with $\dot{\gamma}$, we show in Figure 8 the average number of patches $\langle N_p \rangle$ as well as the average size $\langle S_p \rangle$. For ϕ = 0.01, we find that the number of clusters fluctuates around an average value of 39 and the number of arms in a cluster is slightly higher than 2 regardless of $\dot{\gamma}$. These results seem to indicate that no or little

https://dx.doi.org/10.1021/acs.macromol.0c01365
Macromolecules 2020, 53, 10015−10027

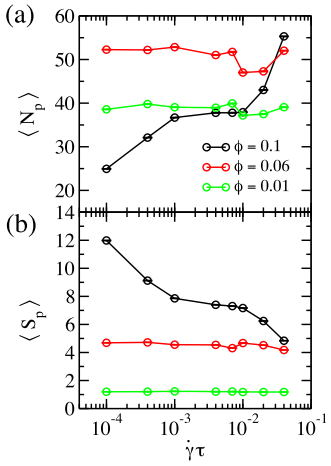

Figure 8. (a) Average number of patches $\langle N_p \rangle$ and (b) average number of arms clustered in a patch $\langle S_p \rangle$ for $\alpha = 0.3$ as a function of shear rate for the three monomer packing fractions indicated in the legend.

changes in this respect occur in the dilute system when shear is applied. We will in short demonstrate that the constant average characteristics of the clusters are actually also almost conserved at the cluster level. At $\phi = 0.1$, $\langle N_p \rangle$ increases with $\dot{\gamma}$, whereas $\langle S_p \rangle$ decreases. This result is consistent with our observation that larger clusters break down into smaller ones as the system is subjected to a higher shear rate. In the intermediate shear regime ($\phi = 0.06$), we observe a constant number of clusters (larger than for the other values of ϕ), which goes a bit down for $\dot{\gamma}\tau \geq 0.01$. This decrease appears not to be accompanied by an increase in average cluster size.

From the previous analysis, two questions arise. The first one is whether the constant average values $\langle N_p \rangle$ and $\langle S_p \rangle$ for the dilute system results in effectively no changes induced by the shear, or of a subtle reorganization of the clusters resulting in the same average parameters. The second question that interests us concerns the change in cluster number and/or size observed for $\phi = 0.06$ and $\phi = 0.1$; are these the results of arms breaking free from the clusters or clusters breaking down into smaller ones? In order to answer these questions, we proceed to plot the cluster size distribution as a function of the number of arms for selected $\dot{\gamma}$ (see Figure 9). For $\phi = 0.01$, the free arms ($S_p = 1$) represent the vast majority of the distribution, followed by two-arm clusters. The number of free arms appears to remain constant with shear, whereas the population of clusters with $S_p \geq 3$ declines slightly while the clusters with $S_p = 2$ become more numerous (Figure 9a).

The changes in the distributions only affect around 1% of the clusters and are therefore not visible in the average values. There are two mechanisms that could affect the distribution in this way: either bigger clusters break into clusters with $S_p = 2$ (which is unlikely because there are also clusters containing an odd S_p) or patches are first broken by shear and then they reform into two-arm aggregates, which is probably the more realistic scenario. For $\phi = 0.06$, as shear increases, we observe that the number of free arms increases at the expense of the bigger clusters ($S_p \geq 3$), the population of two-arm ones increasing slightly. This is consistent with arms being pulled out from clusters by the flow. For $\phi = 0.1$, we also observe an increase with shear in the number of free arms though less important than for $\phi = 0.06$. However, at the same time, the population of small clusters ($2 \leq S_p \leq 6$) grows and the one of

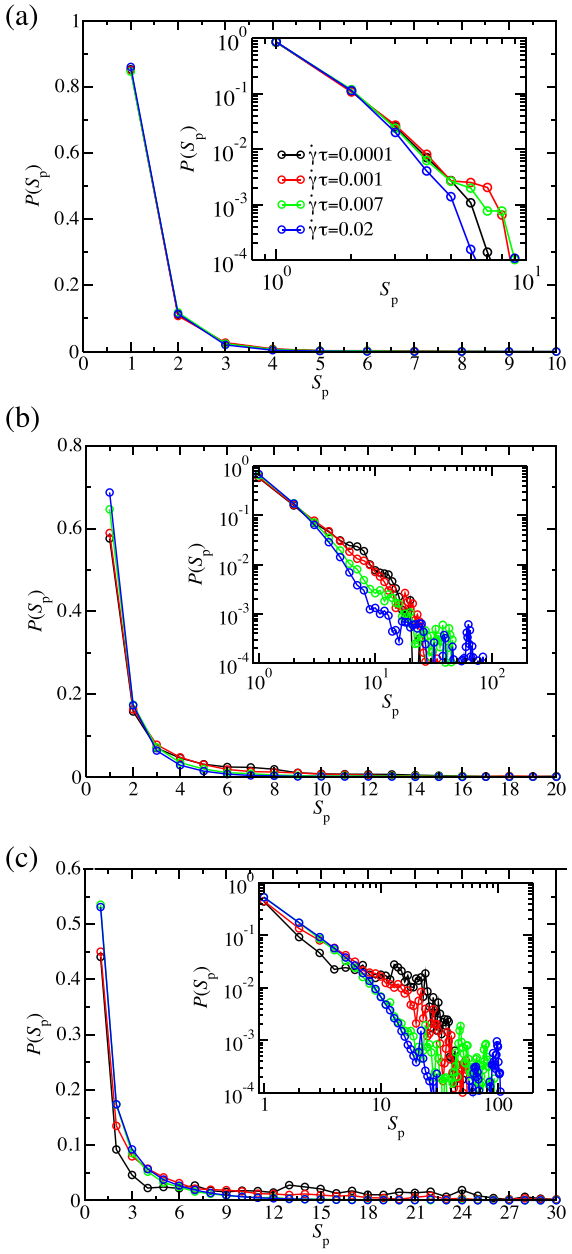

Figure 9. Patch size distribution $P(S_p)$ for $\alpha = 0.3$ and different values of shear rate and monomer volume fraction: (a) $\phi = 0.01$, (b) $\phi = 0.06$, and (c) $\phi = 0.1$. The insets show a log−log representation of $P(S_p)$.

larger clusters go down. At this density, the reorganization of the network seem to be the result of both arms breaking free from the larger-sized cluster but also a result of fragmentation of these clusters. A surprising fact is the similarity of this behavior to that of colloidal gels. Analogous to colloidal gels, that decrease their coordination number when shear becomes high enough,[43,44] the BCS networks sacrifice inter-star connections in order to conformationally adjust to shear.

3.4.1. Connectivity. Another measure of the morphological changes occurring in our BCS systems when shear is applied is related to the connectivity of the system. Groups of connected BCSs at different shear rates and densities are presented in Figure 10. At the lowest density considered, the shape of the connected component as a whole changes when shear is applied, becoming more elongated. The elongation does not

https://dx.doi.org/10.1021/acs.macromol.0c01365
Macromolecules 2020, 53, 10015−10027

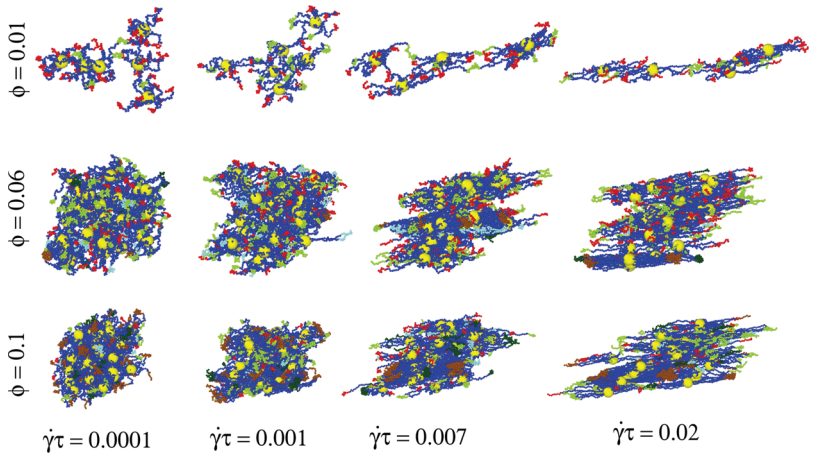

Figure 10. Snapshots of typical groups of connected BCSs for $\alpha = 0.3$ and different shear rates and volume fractions. The nonfunctionalized part of the star is colored in blue, whereas the functionalized blocks have been colored according to the size of the clusters they are part of using the same color code as in Figure 7. To make individual stars easier to visualize, the anchors, which are indicated in yellow, have been drawn at a 4 times larger scale than their actual size.

only come from the stretching of stars but also from reorganization of the inter-star connections. This allows the BCSs to align to the flow, facilitating the movement as a group, while as many inter-star connections as possible are kept. This behavior is consistent with the observed shear banding phenomena. The number of stars per connected component decreases with shear rate because stars that become free at some point in time are carried away by the flow, making their reattachment unlikely. At higher densities, the BCSs appear to form a percolating network, which seems to survive shear. The most interesting phenomenon found is that, when stars elongate under the effect of shear, a sort of stacked configuration is observed, indicating that the stars bring their anchor almost in contact forming a string-like or stack-like structure. The noninteracting part of the stars which are on either side of the anchor also stacks, as well as the attractive parts. This organization was hinted at by the radial correlation functions.

To better understand the changes that shear generates in the structure of the system, we look at the connectivity of the system by measuring the size of the connected components present (i.e., the number of connected stars). In Figure 11, we show the average number of components, the average number of free stars, the average size of the largest component, and the number of free arms for the whole system. We find that except in the dilute system ($\phi = 0.01$), where it is composed out of multiple components (≈6−7) regardless of the shear rate, the system is completely connected up to $\dot{\gamma}\tau = 0.01$. This single component contains all the stars in the system (the number of free stars being zero), indicating that we have a percolation network as we had already hinted in the previous paragraph. At $\phi = 0.1$ and for the higher shear rates, a small number of single BCSs start to fragment from the percolating component, the rest of the stars remaining connected. In addition to the release of a few free stars, at $\phi = 0.06$, the network breaks for $\dot{\gamma}\tau = 0.04$ into two big pieces (≈10−20 stars). The low-density behavior is different: many stars are free (more that 40%) and this further increases with the shear rate. The size of the largest component in the system only contains six to seven stars, which decreases to ≈4 stars for high shear rates.

While the connectivity parameters do not vary drastically for $\phi = 0.01$ and $\phi = 0.1$, at the intermediate density, provided that the shear rate is high enough, the network connectivity undergoes a drastic change: it breaks into two pieces. This breakage is a mechanism to release the stress accumulated in the network because of the deformations induced by shear. At the higher monomer fraction, this phenomenon is not observed for the shear rates studied because the network is stronger, that is, each star has more connections which mechanically reinforce the network.

The number of free arms can offer further clarification on connectivity. For $\phi = 0.01$, each star has, on average, six to seven free arms, which indicates that only two or three are bound. Considering that arms can bind within a star, not only creating inter-star connections, it is to be expected that the size of components is low and the number of free stars is high. At $\phi = 0.06$, around two arms per star are free, whereas at $\phi = 0.1$, only one arm in each stars is unbound. These values increase with the shear rate up to ≈3 and respectively ≈1.5 free arm per star. With such a high number of attached arms, it is natural that we obtain a percolating network.

3.5. Viscosity. A very important macroscopic property of non-Newtonian fluids in general and of (associating) polymer solutions in particular is the viscosity, which bears the signature of the polymer architecture and chemistry. Unlike the previously presented properties that can be challenging to address experimentally, the viscosity can be measured in rheological experiments. Determining this quantity thus provides an important link between microscopic organization of the BCSs and the macroscopic behavior of the material. Here, we calculate the polymer viscosity η_p, which is expected to dominate the total viscosity at sufficiently high concentrations, and which is also responsible for the non-Newtonian linear rheology of the system. To this effect, we calculate the stress tensor $\boldsymbol{\sigma}_p$ that involves kinetic and interaction contributions for the polymer beads, involving exclusively the forces exerted by other beads, and can be conveniently computed via the relation

$$\boldsymbol{\sigma}_p = \frac{1}{V}\left\langle \sum_{i=1}^{N_t} M\tilde{\boldsymbol{v}}_i \otimes \tilde{\boldsymbol{v}}_i + \frac{1}{2}\sum_{i=1,j\neq i}^{N_t} \boldsymbol{r}_{ij} \otimes \boldsymbol{F}_{ij} \right\rangle \quad (12)$$

Here, $M = 5m$ is the monomer mass, $V = {L_{box}}^3$ is the volume of the simulation box, $N_t = N_s N_{mon}$ is the total number of

https://dx.doi.org/10.1021/acs.macromol.0c01365
Macromolecules 2020, 53, 10015−10027

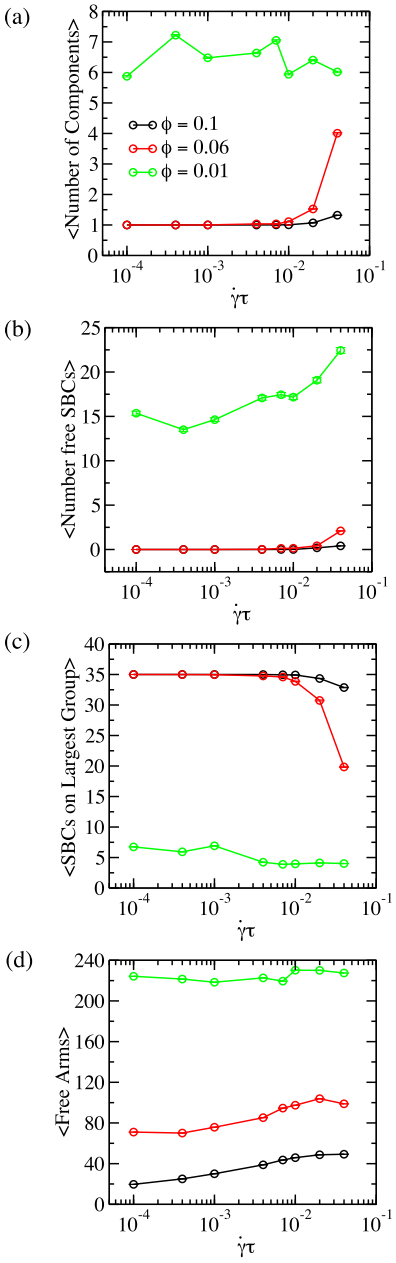

Figure 11. Connectivity parameters as a function of shear rate for α = 0.3 and different concentrations: (a) average number of components, (b) average number of free stars, (c) average size of the largest component, and (d) average number of free arms.

monomers, $\tilde{\boldsymbol{v}}_i = \boldsymbol{v}_i - \dot{\gamma} y_i \hat{\boldsymbol{x}}$ is the peculiar velocity of the i-th monomer, $\mathbf{r}_{ij} = \mathbf{r}_i - \mathbf{r}_j$ and $\mathbf{F}_{ij}$ are the pair monomer−monomer forces, including both FENE and Lennard-Jones-like contributions. It is to note that for our system, the kinetic contribution to the stress tensor is several orders of magnitude smaller than the interaction term.

In Figure 12, we present the polymer viscosity $\eta_p = \sigma_{p;xy}/\dot{\gamma}$ as a function of shear rate $\dot{\gamma}$ at both α = 0.3 and α = 0.5 for the three densities considered. As a general trend, we observe higher viscosity for more concentrated systems and also a shear thinning behavior, that is, a decreasing viscosity as the shear rate increases, for all the systems studied. The two higher monomer fraction systems (ϕ = 0.1 and ϕ = 0.06) feature a very similar behavior. At low shear rates, the systems with α = 0.5 exhibit a stronger shear thinning. For $\dot{\gamma}\tau \geq 0.01$, the curves

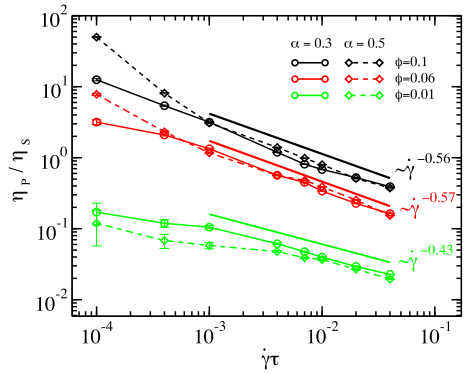

Figure 12. Polymer viscosity η_p, expressed in units of solvent viscosity η_s, as a function of shear rate for the systems under consideration.

for both α-s collapse, the slopes being very similar (−0.56 and −0.57, respectively). For the dilute systems, we also observed a collapse of the two curves for high $\dot{\gamma}$; however, the slope is only −0.43. This last result is slightly higher than the values reported in the literature for semidilute solutions of stars with less than 50 arms.[52] Compared to nonaggregating stars, which also exhibit a power law decay for high enough shear rates with concentration-dependent exponent ranging from −0.3 for a dilute system to −0.4 for a system above overlap concentration,[34] BCSs exhibit a stronger shear thinning, which results from a combination of reorientation of arms and rearranging of inter-star connections.

4. CONCLUSIONS

In this work, we analyzed the global structure, patchiness, and viscosity of suspensions of star-shaped block copolymers (BCS) under shear flow. Following recent studies on the self-assembly and network formation in low-functionality BCS systems,[13] we explored their nonequilibrium behavior from semidilute ($\phi/\phi^* \simeq 0.1$) to concentrated ($\phi/\phi^* \simeq 1.1$) regimes. As previously described,[13] the chosen parameters, that is, functionality, amphiphilicity, and attraction strength between solvophobic segments, lead the system to the formation of homogeneous percolating networks, whose patchiness, morphology, and connectivity are significantly reorganized by the shear rate. As the latter increases, the BCSs in the network elongate in the shear direction and shrink in the other two, compelling the larger clusters of B-monomers (patches) to break up into smaller ones. This effect becomes more important as the concentration increases (see Figure 8), leading to the rising of the number of patches but of a smaller size. Also, a stacked configuration of BCSs is observed, which allows the star cores to aligning in a stack-like structure, which is reminiscent of the scaffold-like structures observed in rigid, linear telechelic polymers.[17]

Regarding the viscosity of the system, more inter-star association takes place as the concentration increases, leading to an increasing zero-shear viscosity.[16] As shear enters into play, the breaking of patches plus the BCS reorientation results into thixotropic behavior (shear thinning) with the thinning exponent growing in magnitude with the concentration of the solution. The stars reorganize significantly during shear and change morphology. This could be interesting for experimental application perspective because anchors could be functionalized in such a way that they have an extra linking possibility to reinforce the network.

https://dx.doi.org/10.1021/acs.macromol.0c01365
Macromolecules 2020, 53, 10015−10027

AUTHOR INFORMATION

Corresponding Author

Ioana C. Gârlea − *Faculty of Physics, University of Vienna, 1090 Vienna, Austria;* orcid.org/0000-0001-5209-9936; Email: ioana.cristina.garlea@univie.ac.at

Authors

Diego Jaramillo-Cano − *Faculty of Physics, University of Vienna, 1090 Vienna, Austria*

Manuel Camargo − *CICBA & FIMEB, Universidad Antonio Nariño, 760030 Cali, Colombia;* orcid.org/0000-0003-0276-2650

Christos N. Likos − *Faculty of Physics, University of Vienna, 1090 Vienna, Austria;* orcid.org/0000-0003-3550-4834

Complete contact information is available at: https://pubs.acs.org/10.1021/acs.macromol.0c01365

Notes

The authors declare no competing financial interest.

ACKNOWLEDGMENTS

D.J.-C. acknowledges the support by the European Training Network COLLDENSE (H2020-MCSA-ITN-2014, grant no. 642774) and from the Dissertation Completion Fellowship Programme of the University of Vienna. M.C. thanks VCTI-UAN for financial support (Project 2018201). Computer time at the Vienna Scientific Cluster (VSC) is gratefully acknowledged.

REFERENCES

(1) Feng, H.; Lu, X.; Wang, W.; Kang, N.-G.; Mays, J. Block copolymers: Synthesis, self-assembly, and applications. *Polymers* **2017**, *9*, 494.

(2) Atanase, L.; Riess, G. Self-assembly of block and graft copolymers in organic solvents: An overview of recent advances. *Polymers* **2018**, *10*, 62.

(3) Qiang, X.; Chakroun, R.; Janoszka, N.; Gröschel, A. H. Self-Assembly of Multiblock Copolymers. *Isr. J. Chem.* **2019**, *59*, 945−958.

(4) Capone, B.; Coluzza, I.; LoVerso, F.; Likos, C. N.; Blaak, R. Telechelic star polymers as self-assembling units from the molecular to the macroscopic scale. *Phys. Rev. Lett.* **2012**, *109*, 238301.

(5) Rovigatti, L.; Capone, B.; Likos, C. N. Soft self-assembled nanoparticles with temperature-dependent properties. *Nanoscale* **2016**, *8*, 3288−3295.

(6) Hietala, S.; Strandman, S.; Järvi, P.; Torkkeli, M.; Jankova, K.; Hvilsted, S.; Tenhu, H. Rheological properties of associative star polymers in aqueous solutions: Effect of hydrophobe length and polymer topology. *Macromolecules* **2009**, *42*, 1726−1732.

(7) Hadjichristidis, N.; Pitsikalis, M.; Iatrou, H.; Driva, P.; Sakellariou, G.; Chatzichristidi, M. Polymers with Star-Related Structures: Synthesis, Properties, and Applications. *Polym. Sci.* **2012**, *6*, 29−111.

(8) Mortensen, K.; Annaka, M. Structural study of four-armed amphiphilic star-block copolymers: pristine and end-linked tetronic T1307. *ACS Macro Lett.* **2016**, *5*, 224−228.

(9) Cao, M.; Nie, H.; Hou, Y.; Han, G.; Zhang, W. Synthesis of star thermoresponsive amphiphilic block copolymer nano-assemblies and the effect of topology on their thermoresponse. *Polym. Chem.* **2019**, *10*, 403−411.

(10) Moghimi, E.; Chubak, I.; Statt, A.; Howard, M. P.; Founta, D.; Polymeropoulos, G.; Ntetsikas, K.; Hadjichristidis, N.; Panagiotopoulos, A. Z.; Likos, C. N.; Vlassopoulos, D. Self-Organization and Flow of Low-Functionality Telechelic Star Polymers with Varying Attraction. *ACS Macro Lett.* **2019**, *8*, 766−772.

(11) Apostolides, D. E.; Sakai, T.; Patrickios, C. S. Dynamic covalent star poly (ethylene glycol) model hydrogels: A new platform for mechanically robust, multifunctional materials. *Macromolecules* **2017**, *50*, 2155−2164.

(12) Gârlea, I. C.; Bianchi, E.; Capone, B.; Rovigatti, L.; Likos, C. N. Hierarchical self-organization of soft patchy nanoparticles into morphologically diverse aggregates. *Curr. Opin. Colloid Interface Sci.* **2017**, *30*, 1−7.

(13) Gârlea, I. C.; Jaramillo-Cano, D.; Likos, C. N. Self-organization of gel networks formed by block copolymer stars. *Soft Matter* **2019**, *15*, 3527−3540.

(14) Seiffert, S.; Sprakel, J. Physical Chemistry of Supramolecular Polymer Networks. *Chem. Soc. Rev.* **2012**, *41*, 909−930.

(15) Grillet, A. M.; Wyatt, N. B.; Gloe, L. M. In *Rheology*; De Vicente, J., Ed.; InTech Croatia, 2012; Chapter 3, pp 59−80.

(16) Chassenieux, C.; Nicolai, T.; Benyahia, L. Rheology of associative polymer solutions. *Curr. Opin. Colloid Interface Sci.* **2011**, *16*, 18−26.

(17) Taslimi, F.; Gompper, G.; Winkler, R. G. Scaffold structures by telechelic rodlike polymers: Nonequilibrium structural and rheological properties under shear flow. *Macromolecules* **2014**, *47*, 6946−6954.

(18) Myung, J. S.; Winkler, R. G.; Gompper, G. Self-organization in suspensions of end-functionalized semiflexible polymers under shear flow. *J. Chem. Phys.* **2015**, *143*, 243117.

(19) Metri, V.; Louhichi, A.; Yan, J.; Baeza, G. P.; Matyjaszewski, K.; Vlassopoulos, D.; Briels, W. J. Physical networks from multifunctional telechelic star polymers: A rheological study by experiments and simulations. *Macromolecules* **2018**, *51*, 2872−2886.

(20) Vlassopoulos, D.; Cloitre, M. Tunable rheology of dense soft deformable colloids. *Curr. Opin. Colloid Interface Sci.* **2014**, *19*, 561−574.

(21) Jaramillo-Cano, D.; Formanek, M.; Likos, C. N.; Camargo, M. Star block-copolymers in shear flow. *J. Phys. Chem. B* **2018**, *122*, 4149−4158.

(22) Wadgaonkar, I.; Chatterji, A. Network formation and gelation in telechelic star polymers. *J. Chem. Phys.* **2017**, *146*, 084906.

(23) Malevanets, A.; Kapral, R. Mesoscopic model for solvent dynamics. *J. Chem. Phys.* **1999**, *110*, 8605−8613.

(24) Malevanets, A.; Kapral, R. Solute molecular dynamics in a mesoscale solvent. *J. Chem. Phys.* **2000**, *112*, 7260−7269.

(25) Frenkel, D.; Smit, B. *Understanding Molecular Simulation: from Algorithms to Applications*; Elsevier, 2001; Vol. *1*.

(26) Gompper, G.; Ihle, T.; Kroll, D.; Winkler, R. *Advanced Computer Simulation Approaches for Soft Matter Sciences III*; Springer, 2009; pp 1−87.

(27) Lees, A. W.; Edwards, S. F. The computer study of transport processes under extreme conditions. *J. Phys. C: Solid State Phys.* **1972**, *5*, 1921.

(28) Evans, D.; Morriss, G.; Craig, D.; McWeeny, R. *Statistical Mechanics of Nonequilibrium Liquids; Theoretical Chemistry*; Elsevier Science, 2013.

(29) Ripoll, M.; Winkler, R.; Gompper, G. Star polymers in shear flow. *Phys. Rev. Lett.* **2006**, *96*, 188302.

(30) Doi, M.; Edwards, S. *The Theory of Polymer Dynamics; Comparative Pathobiology—Studies in the Postmodern Theory of Education*; Clarendon Press, 1988.

(31) Steinhauser, M. O. A molecular dynamics study on universal properties of polymer chains in different solvent qualities. Part I. A review of linear chain properties. *J. Chem. Phys.* **2005**, *122*, 094901.

(32) Zifferer, G.; Preusser, W. Monte Carlo simulation studies of the size and shape of ring polymers. *Macromol. Theory Simul.* **2001**, *10*, 397−407.

(33) Theodorou, D. N.; Suter, U. W. Detailed molecular structure of a vinyl polymer glass. *Macromolecules* **1985**, *18*, 1467−1478.

(34) Fedosov, D. A.; Singh, S. P.; Chatterji, A.; Winkler, R. G.; Gompper, G. Semidilute solutions of ultra-soft colloids under shear flow. *Soft Matter* **2012**, *8*, 4109−4120.

(35) Latinwo, F.; Hsiao, K.-W.; Schroeder, C. M. Nonequilibrium thermodynamics of dilute polymer solutions in flow. *J. Chem. Phys.* **2014**, *141*, 174903.

(36) Latinwo, F.; Schroeder, C. M. Determining elasticity from single polymer dynamics. *Soft Matter* **2014**, *10*, 2178−2187.
(37) Huang, C.-C.; Winkler, R. G.; Sutmann, G.; Gompper, G. Semidilute polymer solutions at equilibrium and under shear flow. *Macromolecules* **2010**, *43*, 10107−10116.
(38) Baig, C.; Mavrantzas, V. G.; Kröger, M. Flow effects on melt structure and entanglement network of linear polymers: Results from a nonequilibrium molecular dynamics simulation study of a polyethylene melt in steady shear. *Macromolecules* **2010**, *43*, 6886−6902.
(39) Mai, D. J.; Marciel, A. B.; Sing, C. E.; Schroeder, C. M. Topology-controlled relaxation dynamics of single branched polymers. *ACS Macro Lett.* **2015**, *4*, 446−452.
(40) Jeong, S. H.; Kim, J. M.; Baig, C. Rheological influence of short-chain branching for polymeric materials under shear with variable branch density and branching architecture. *Macromolecules* **2017**, *50*, 4491−4500.
(41) Hsiao, K.-W.; Schroeder, C. M.; Sing, C. E. Ring polymer dynamics are governed by a coupling between architecture and hydrodynamic interactions. *Macromolecules* **2016**, *49*, 1961−1971.
(42) Yoon, J.; Kim, J.; Baig, C. Nonequilibrium molecular dynamics study of ring polymer melts under shear and elongation flows: A comparison with their linear analogs. *J. Rheol.* **2016**, *60*, 673−685.
(43) Colombo, J.; Del Gado, E. Stress localization, stiffening, and yielding in a model colloidal gel. *J. Rheol.* **2014**, *58*, 1089−1116.
(44) Jamali, S.; McKinley, G. H.; Armstrong, R. C. Microstructural rearrangements and their rheological implications in a model thixotropic elastoviscoplastic fluid. *Phys. Rev. Lett.* **2017**, *118*, 048003.
(45) Sablić, J.; Praprotnik, M.; Delgado-Buscalioni, R. Deciphering the dynamics of star molecules in shear flow. *Soft Matter* **2017**, *13*, 4971−4987.
(46) Myung, J. S.; Taslimi, F.; Winkler, R. G.; Gompper, G. Self-Organized Structures of Attractive End-Functionalized Semiflexible Polymer Suspensions. *Macromolecules* **2014**, *47*, 4118−4125.
(47) Allen, M.; Tildesley, D. *Computer Simulation of Liquids*; Oxford Science Publications, Clarendon Press, 1987.
(48) Stellbrink, J.; Lonetti, B.; Rother, G.; Willner, L.; Richter, D. Shear induced structures of soft colloids: Rheo-SANS experiments on kinetically frozen PEP−PEO diblock copolymer micelles. *J. Phys.: Condens. Matter* **2008**, *20*, 404206.
(49) Calabrese, M. A.; Rogers, S. A.; Murphy, R. P.; Wagner, N. J. The rheology and microstructure of branched micelles under shear. *J. Rheol.* **2015**, *59*, 1299−1328.
(50) Liberatore, M. W.; Nettesheim, F.; Wagner, N. J.; Porcar, L. Spatially resolved small-angle neutron scattering in the 1-2 plane: A study of shear-induced phase-separating wormlike micelles. *Phys. Rev. E: Stat., Nonlinear, Soft Matter Phys.* **2006**, *73*, 020504.
(51) Förster, S.; Konrad, M.; Lindner, P. Shear thinning and orientational ordering of wormlike micelles. *Phys. Rev. Lett.* **2005**, *94*, 017803.
(52) Singh, S. P.; Chatterji, A.; Gompper, G.; Winkler, R. G. Dynamical and rheological properties of ultrasoft colloids under shear flow. *Macromolecules* **2013**, *46*, 8026−8036.

https://dx.doi.org/10.1021/acs.macromol.0c01365
Macromolecules 2020, 53, 10015−10027